

Very long baseline interferometry detection of nearby (< 100 pc) young stars

Pilot observations

Sergio A. Dzib¹, Laurent Loinard², Ralf Launhardt³, and Jazmín Ordóñez-Toro²

¹ Max-Planck-Institut für Radioastronomie, Auf dem Hügel 69, D-53121 Bonn, Germany

² Instituto de Radioastronomía y Astrofísica, Universidad Nacional Autónoma de México, 58090, Morelia, Michoacán, Mexico

³ Max-Planck-Institut für Astronomie, Königstuhl 17, D-69117 Heidelberg, Germany

March 29, 2024

ABSTRACT

To increase the number of sources with very long baseline interferometry (VLBI) astrometry available for comparison with the *Gaia* results, we have observed 31 young stars with recently reported radio emission. These stars are all in the *Gaia* DR3 catalog and were suggested, on the basis of conventional interferometry observations, to be nonthermal radio emitters and are therefore good candidates for VLBI detections. The observations were carried out with the Very Long Baseline Array (VLBA) at two epochs separated by a few days and yielded ten detections (a roughly 30% detection rate). Using the astrometric *Gaia* results, we extrapolated the target positions to the epochs of our radio observations and compared them with the position of the radio sources. For seven objects, the optical and radio positions are coincident within five times their combined position errors. Three targets, however, have position discrepancies above eight times the position errors, indicating different emitting sources at optical and radio wavelengths. In one case, the VLBA emission is very likely associated with a known companion of the primary target. In the two other cases, we associated the VLBA emission with previously unknown companions, but further observations will be needed to confirm this.

Key words. astrometry — techniques: interferometry — radiation mechanisms: non-thermal — stars:kinematics

1. Introduction

Stellar radio astrometry with very long baseline interferometry (VLBI) at centimeter wavelengths achieves angular resolutions of a few milli-arcseconds and an astrometric accuracy on the order of 0.1 mas (e.g., Reid & Honma 2014). For young stars, VLBI radio astrometry has primarily been used to better constrain star-forming region distances, which were poorly known at the time or were debated due to discrepant results from indirect methods (e.g., Loinard et al. 2005, 2007; Dzib et al. 2010; Ortiz-León et al. 2017b). In young stars, radio emission detectable with VLBI is nonthermal and is produced in stellar coronae (Güdel 2002) that typically extend up to a few radii and remain unresolved with VLBI observations at centimeter wavelengths. Thus, the astrometry derived from these radio observations directly traces the stellar motion. Recently, the *Gaia* mission (Gaia Collaboration et al. 2016, 2021, 2023) has been delivering astrometry of over a billion stars, including many nearby young stars. Not surprisingly, *Gaia* results have confirmed the astrometric results previously reported using the VLBI technique (e.g., Ortiz-León et al. 2018; Galli et al. 2019).

Gaia and VLBI astrometry accuracies are comparable, so the two techniques are complementary (e.g. Dzib et al. 2021). Comparing trigonometric parallaxes measured with both can constrain the *Gaia* zero-point offset (Lindgren et al. 2018; Lindgren 2020; Riess et al. 2018; Zinn et al. 2019; Xu et al. 2019). Also, high precision VLBI astrometry allows for the linking of the optical stellar reference frames to the radio extragalactic reference frame since VLBI stellar astrometry is relative to them (Lestrade et al. 1999). Recently, Lindgren (2020) analyzed 41

stars in the *Gaia* catalog with existing VLBI stellar astrometry. He noticed discrepancies between the VLBI and *Gaia*-derived astrometry and rejected 15 stars for further analysis. These rejected stars are binary and multiple systems that do not comply with the linear motion prescription currently used for *Gaia* astrometry. From the remaining 26 stars, he estimated the rotation of the *Gaia* bright stars ($G \leq 13$ mag) reference frame with respect to the distant quasar frame (the so-called *Gaia* Celestial Reference Frame). Lindgren (2020) recognized that stellar VLBI astrometry can provide independent astrometric results that could be used to test results from current and future *Gaia* releases. He also noted that for this purpose, it will be necessary to re-observe stars with VLBI and identify new stars that can be detected with the VLBI technique. There are, however, few stars with suspected nonthermal radio emission that have not already been observed with the VLBI technique.

Looking to increase the number of stars with both VLBI and *Gaia* astrometry, the main goal of the present work is to obtain VLBI observations of nearby young stars with suspected non-thermal radio emission and compare their positions with those reported by *Gaia*. Here we report VLBI observations of 31 nearby (< 100 pc) young stars (< 100 Myr) that were recently reported to be radio emitters by Launhardt et al. (2022). These authors also suggested that the radio emission is likely of non-thermal nature and could thus be detected with VLBI observations. The stars have optical counterparts, and most of them are bright stars in the *Gaia* catalog. In Table 1, these stars are listed together with their astrometric solution from *Gaia* DR3 (Gaia Collaboration et al. 2021, 2023) and other known properties.

Table 1. Target sources.

Star ID	R.A. (J2016.0) ($^{\circ}$)	Dec. (J2016.0) ($^{\circ}$)	π (mas)	Dist. (pc)	$\mu_{\alpha} \cdot \cos(\delta)$ (mas yr $^{-1}$)	μ_{δ} (mas yr $^{-1}$)	spT	age (Myr)	age ref.	G (mag)	Dates for Max. Parallax	Obs. Group	Phase Cal.	Separation ($^{\circ}$)
BD+17 232	024.4144646604	+018.5922019429	18.95 \pm 00.03	52.77 \pm 00.09	73.79 \pm 00.04	-43.35 \pm 00.03.	K3VE	10	1	10.18	Jan 16 - Jul 18	A	J0139+1753	0.9
HIP 12545	040.3582211403	+005.9881913726	22.58 \pm 00.02	44.30 \pm 00.04	79.07 \pm 00.02	-56.70 \pm 00.02.	K6Ve	10	2	9.82	Feb 2 - Aug 4	B	J0239+0416	1.8
HIP 12635	040.5877605186	+038.6220662083	20.09 \pm 00.02	49.78 \pm 00.05	82.11 \pm 00.02	-107.55 \pm 00.02.	K2V	149	3	9.92	Feb 2 - Aug 5	B	J0253+3835	2.1
V 875 Per	043.0736090107	+036.2798896433	04.07 \pm 00.02	245.92 \pm 01.08	52.87 \pm 00.02	-38.55 \pm 00.02	K2IV	63	4	10.45	Feb 4 - Aug 7	B	J0246+3536	1.4
TYC 3301-2585-1 ^a	043.9317736370	+047.7795639137	19.97 \pm 00.02	50.07 \pm 00.05	85.50 \pm 00.02	-79.53 \pm 00.02	K5Ve	42	3	10.71	Feb 5 - Aug 8	B	J0303+4716	1.4
HD 22213	053.5684734519	-012.0688463141	19.46 \pm 00.02	51.38 \pm 00.05	74.46 \pm 00.02	-34.36 \pm 00.01	G7V	45	3	8.58	Feb 15 - Aug 18	C	J0336-1302	1.1
HD 23524 ^b	057.0963206572	+052.0375180643	19.35 \pm 01.62	51.85 \pm 04.50	61.87 \pm 01.98	-70.99 \pm 01.67	K1V	42	3	8.62	Feb 18 - Aug 21	D	J0350+5138	0.5
HD 24681	058.8352088930	-001.7296295356	17.94 \pm 00.02	55.73 \pm 00.06	43.50 \pm 00.02	-91.47 \pm 00.02	G8V	149	3	8.79	Feb 20 - Aug 23	C	J0351-0301	1.7
HD 285281	060.1294810416	+019.5890872952	07.34 \pm 00.02	136.22 \pm 00.43	04.04 \pm 00.03	-12.36 \pm 00.02	K1	1.5	4	9.97	Feb 21 - Aug 24	D	J0401+2110	1.6
HD 284135 ^c	061.4191041862	+022.8032778542	12.50 \pm 01.00	80.69 \pm 06.55	05.50 \pm 01.00	-14.70 \pm 01.00	G3V:	1.5	1	9.17	Feb 22 - Aug 25	D	J0412+2305	1.7
HD 31281	073.7900713168	+018.4419023094	08.25 \pm 00.03	121.29 \pm 00.43	-2.51 \pm 00.04	-16.10 \pm 00.02	G1V:	1.5	5	9.06	Mar 6 - Sep 6	E	J0449+1754	1.5
BD-08 995	074.7023574082	-008.7277965955	11.47 \pm 00.02	87.15 \pm 00.12	25.83 \pm 00.01	-21.61 \pm 00.01	K0V	42	3,6	10.00	Mar 7 - Sep 7	E	J0457-0849	0.4
HD 286264	075.2054343407	+015.4499325911	18.83 \pm 00.02	53.09 \pm 00.04	18.31 \pm 00.02	-58.72 \pm 00.01	K2IV	24	3	10.37	Mar 7 - Sep 8	E	J0459+1438	0.9
HD 293857 ^d	077.7903401655	-004.1820005272	12.82 \pm 01.00	78.45 \pm 06.24	18.70 \pm 01.00	-57.50 \pm 01.00	G8V	24	3	9.04	Mar 10 - Sep 10	E	J0505-0419	1.3
TYC 713-661-1	084.2085922983	+013.6317744334	17.61 \pm 00.02	56.77 \pm 00.06	04.90 \pm 00.02	-109.84 \pm 00.01	K0V	149	3	10.16	Mar 16 - Sep 16	F	J0539+1433	1.2
TYC 5925-1547-1	084.8465611076	-019.5583471893	14.30 \pm 00.17	69.95 \pm 00.82	21.30 \pm 00.13	-48.63 \pm 00.16	K1V	150	3,6	10.28	Mar 16 - Sep 17	F	J0536-2005	0.9
AI Lep	085.0864740191	-019.6697559694	13.86 \pm 00.01	72.16 \pm 00.07	19.32 \pm 00.01	-11.69 \pm 00.01	G2V	42	3	8.94	Mar 17 - Sep 17	F	J0536-2005	1.0
HD 62237	115.6106888262	-016.2834934596	08.02 \pm 00.10	124.76 \pm 01.60	-9.44 \pm 00.09	-13.21 \pm 00.09	G5V	42	3,6	9.39	Apr 14 - Oct 16	G	J0746-1555	1.0
SAO 135659	123.4623602751	-007.6403837042	19.97 \pm 00.20	50.07 \pm 00.51	-32.15 \pm 00.23	-32.31 \pm 00.19	K0	42	3	9.01	Apr 22 - Oct 23	G	J0808-0751	1.4
WDS 09035+3750 B	135.8623936283	+037.8407266874	32.75 \pm 00.12	30.54 \pm 00.11	-65.85 \pm 00.11	-163.11 \pm 00.08	M3-6V	42	3	6.91	May 4 - Nov 5	H	J0850+3747	2.6
HD 82159	142.6484056528	+010.6016777097	28.23 \pm 00.04	35.43 \pm 00.05	-200.06 \pm 00.04	-12.88 \pm 00.03	G9V	150	7	8.41	May 11 - Nov 11	H	J0935+0915	1.8
HD 82558	143.1054112092	-011.1844843913	54.74 \pm 00.02	18.27 \pm 00.01	-248.04 \pm 00.02	34.28 \pm 00.02	K0V	43	8	7.50	May 12 - Nov 12	H	J0933-1139	0.6
GJ 2079	153.5792772472	+021.0741011408	42.74 \pm 01.00	23.41 \pm 00.55	-119.55 \pm 01.00	-191.19 \pm 01.00	M0.7V	24	3	9.36	May 23 - Nov 23	H	J1016+2037	0.7
HD 135363	226.9819941355	+076.2014908036	33.71 \pm 00.05	29.66 \pm 00.05	-127.19 \pm 00.08	165.47 \pm 00.07	G5V	45	9	8.39	Feb 8 - Aug 11	I	J1448+7601	1.2
UCAC4 832-014013	226.9860077519	+076.2338226259	33.71 \pm 00.03	29.66 \pm 00.02	-127.64 \pm 00.04	163.10 \pm 00.04	M4.5V	12.40	Feb 8 - Aug 11	I	J1448+7601	1.2
HD 199143	313.9489042861	-017.1144445844	21.78 \pm 00.03	45.91 \pm 00.07	55.73 \pm 00.03	-58.67 \pm 00.03	F8	24	3	7.32	May 2 - Nov 3	J	J2107-1708	2.7
HD 358623	314.0116622465	-017.1818893172	21.70 \pm 00.02	46.08 \pm 00.05	57.32 \pm 00.02	-62.20 \pm 00.02	K6Ve	24	3	9.90*	May 2 - Nov 3	J	J2107-1708	2.7
SAO 50350	315.1960688588	+045.5029486058	19.31 \pm 00.01	51.78 \pm 00.03	38.84 \pm 00.01	08.50 \pm 00.01	F8	200	8	8.36	May 4 - Nov 4	J	J2102+4702	1.6
GJ 4199	322.7577934607	+023.3347377313	41.29 \pm 00.02	24.22 \pm 00.01	134.65 \pm 00.01	-144.89 \pm 00.01	K5Ve	149	3	8.85	May 11 - Nov 12	K	J2125+2442	1.9
SAO 51891	335.0299106318	+049.5033014554	29.07 \pm 00.02	34.40 \pm 00.02	93.24 \pm 00.02	07.37 \pm 00.02	K1V	37	8	8.22	May 24 - Nov 24	K	J2201+5048	3.2
SAO 108142	341.1734897431	+017.9047178334	20.85 \pm 00.07	47.97 \pm 00.17	82.49 \pm 00.08	-82.11 \pm 00.07	K0	149	3	9.17	May 31 - Dec 1	K	J2242+1741	0.5

Notes. Stars with a detected radio source in this work are highlighted. The positions, parallax, and proper motion were obtained from the *Gaia* DR3 catalog (Gaia Collaboration et al. 2021, 2023), with some exceptions.

^(a) Hereafter TYC 3301. ^(b) Star in *Gaia* DR3 without parallax and proper motions. Position is from *Gaia* DR3, and parallax and proper motions are taken from the Hipparcos catalog (van Leeuwen 2007). ^(c) Star in *Gaia* DR3 catalog without parallax and proper motions. Position is from *Gaia* DR3, proper motions are from Tycho-2 catalog (Høg et al. 2000) and distance information from Carpenter et al. (2009). ^(d) Star in *Gaia* DR3 catalog without parallax and proper motions. Position is from *Gaia* DR3, proper motions are from the Tycho-2 catalog, and distance information is from da Silva et al. (2009). The last column lists the angular separation between the target source and the phase calibrator.

Age references: (1) Galicher et al. (2016), (2) Weise et al. (2010), (3) Bell et al. (2015), (4) Carpenter et al. (2009), (5) Kenyon & Hartmann (1995), (6) da Silva et al. (2009), (7) Desidera et al. (2015), (8) Stanford-Moore et al. (2020), and (9) Montes et al. (2001).

2. Observations

The observations were obtained at 20 epochs in the first half of 2021 with the Very Long Baseline Array (VLBA) using the C-band receivers ($\lambda = 6.0$ cm; $\nu = 4.8$ GHz). This band was selected as a compromise between the angular resolution, strength of radio fluxes, and the high sensitivity offered by this band. We used the newly offered recording bit rate of 4 Gbps, which improves the sensitivity of the array by a factor of $\sqrt{2}$ with respect to the previous system for an equal observing time. For the present observations, about 45 minutes were spent on each target source per observation, expecting a noise level of $19 \mu\text{Jy beam}^{-1}$, while with the previous system was $27 \mu\text{Jy beam}^{-1}$.

2.1. Observation strategy

The radio emission from the stars in our sample is known to be rapidly variable, and thus we scheduled two observing runs separated by a few days to increase the chances of detection. The observations were scheduled close to the maximum trigonometric parallax extension in right ascension so that they could be combined with future observations to measure the trigonometric parallaxes of the detected sources. The observing dates are listed individually for all 31 radio stars in Table 2.

As the target sources are weak, phase-referencing was used (e.g., Lestrade et al. 1990; Beasley & Conway 1995). This means that the target observing scans (2 min.) are bracketed with scans (1 min.) on a relatively bright quasar with an angular separation of $\lesssim 3^\circ$. The phase corrections determined for the quasar were transferred to the target so the target source positions are referenced to the quasars. The use of this technique, including antenna slewing time, increases the total telescope time by 60% (for instance, for 30 minutes on source, we would need 48 minutes in total). Additionally, to reduce the impact of errors in the troposphere models used by the correlator, we observed so-called geodetic blocks (i.e., ~ 15 -minute blocks at the beginning and/or middle and/or end of the observation) dedicated to observations of five to six bright quasars distributed over the entire sky (Reid & Brunthaler 2004).

To reduce the overheads caused by the geodetic blocks, we organized the targets into 11 groups of sources with similar right ascensions (and therefore also similar dates of maximum parallax elongation). We named these groups using alphabetic letters from A to K. We have one group of one target, three groups of two targets, four groups of three targets, and three groups of four targets (see Table 2). For the groups with one and two targets, we used two geodetic blocks (at the beginning and the end of the session). For groups with three or four targets, we used three geodetic blocks (at the beginning, middle, and end of the sessions). A second advantage of the grouping strategy is that we could schedule the observations such that the (u, v) plane coverage is maximized. This was achieved by intertwining several blocks of 24 minutes of the different sources with similar right ascension throughout the duration of the session.

2.2. Calibration and imaging

The data were edited and calibrated using the software Astronomical Image Processing System (AIPS; Greisen 2003). After a detailed inspection, flawed data were removed. The data were calibrated following the standard schemes plus a calibration of the group delay (i.e., the rate of phase change with frequency). The calibration of the group delay was used to further reduce systematic errors caused by tropospheric zenith delays and iono-

Table 2. Observed epochs.

Group	Epoch 1 yyyy/mm/dd	Epoch 2 yyyy/mm/dd	No. observed targets
A	2021/07/15	2021/07/17	1
B	2021/01/22	2021/01/24	4
C	2021/02/10	2021/02/13	2
D	2021/02/12	2021/02/14	3
E	2021/03/09	2021/03/10	4
F	2021/03/12	2021/03/13	3
G	2021/04/14	2021/04/16	2
H	2021/05/16	2021/05/23	4
I	2021/01/29	2021/01/30	2
J	2021/05/07	2021/05/10	3
K	2021/05/21	2021/05/22	3

Notes. Columns are (from left to right) the name of the group, the two epochs of the observation in civil dates, and the number of targets included in the corresponding group.

spheric content delays (Reid & Brunthaler 2004). With this purpose, we additionally observed ICRF quasars distributed over the sky over a wide range of frequencies (also known as the geodetic blocks; Reid & Brunthaler 2004). First, the geodetic block data were calibrated using a standard procedure. Second, the clock delays and tropospheric terms were derived using the AIPS task DELZN and applied to the target data set using the CALIB. A detailed description of the calibration strategy has been summarized by Loinard et al. (2007); Dzib et al. (2010) and Ortiz-León et al. (2017b).

After calibration, the data were imaged in two steps. First, for the detection experiment, the (u, v) data of the two epochs for each target were combined using the task DBCON in AIPS. This was done with the purpose of decreasing the noise level in the images (by a factor of $\sqrt{2}$) and increasing the chances of detections. Some of the target sources have very high proper motion (up to 250 mas yr^{-1} , see Table 1), so before concatenating the data of the two observed epochs, we corrected the position of the second epoch to coincide with that of the first epoch. This procedure is described in Appendix A. After the concatenation of the two epochs, we imaged large areas around the expected positions of the target sources. These images are $2'' \times 2''$ with 4096 pixels, $500 \mu\text{as}$ each, along both directions, and they used a natural weighting scheme (*Robust=5* in AIPS).¹

In the second step, a new image was obtained for each source around the peak emission on the first image. These new images are $0.1'' \times 0.1''$ with 1024 pixels, $100 \mu\text{as}$ each, and they also used natural weighting. We consider a source detection when the peak value has a signal-to-noise ratio (SNR) > 6.5 in this last image (see discussion by Forbrich et al. 2021). The final images were produced at the position of the detected sources in each of the data sets of individual epochs using the parameters of the previous image. Only in two cases was the detected emission strong enough (with $S/N > 20$) that we could produce final images using an intermediate weighting scheme between natural and uniform (*Robust=0* in AIPS; Briggs 1995) and ob-

¹ The robust scheme weights the visibilities considering the length of the baselines. A natural weighting scheme can be set with *Robust=5* in AIPS and gives more weight to the interferometer's shortest baselines. A uniform scheme weights all the baselines equally and is set with *Robust=-5* in AIPS. The first scheme resulted in images with better sensitivity, and the second scheme resulted in the smallest synthesized beam but with higher noise.

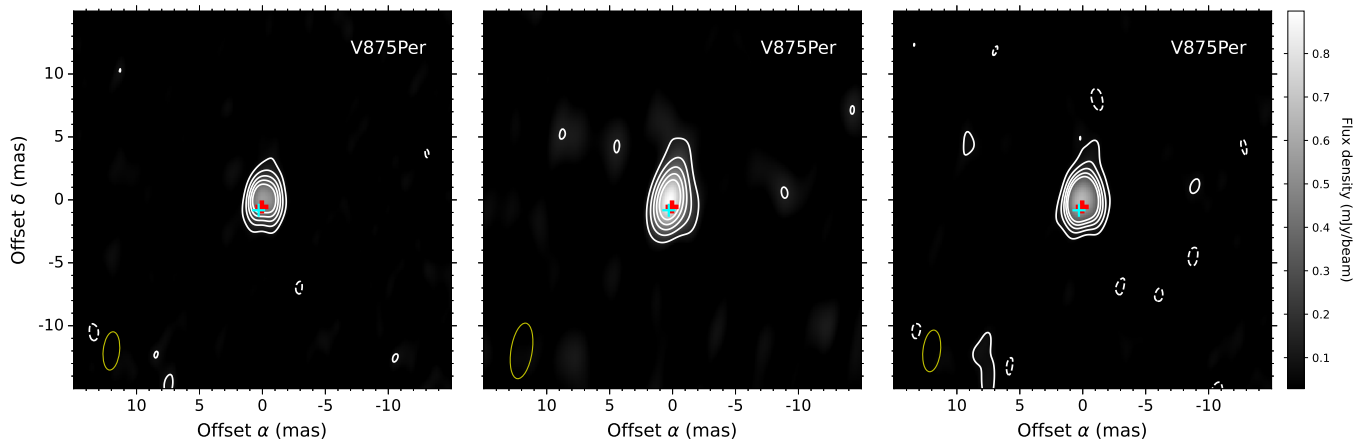


Fig. 1. VLBA images of the radio source related to V 875 Per. The images are centered in the position of the radio source as detected in the first epoch (see Table 4). Images, from left to right, correspond to epochs 1, 2, and the combination of both epochs. Contour levels are $-3, 3, 6, 9, 12,$ and 15 times the noise level of the image as listed in Table 3. The yellow open ellipse in the bottom-left corner represents the size of the synthesized beam of the image as listed in Table 3. The predicted optical position in epochs 1 and 2 are shown as red and cyan crosses, respectively.

tain a better position measurement. The rms noise levels in the final images are $\sim 20 \mu\text{Jy beam}^{-1}$, similar to the VLA images reported by Launhardt et al. (2022). The flux densities and positions of the detected sources were measured using a two-dimensional Gaussian fitting procedure (task JMFIT in AIPS). Statistical errors resulting from JMFIT are given for each detection in columns (4) and (6) in Table 4. Additionally, systematic residual phase errors caused by the transfer of the calibration from the phase calibrator to the target were expected. These errors are on the order of 0.1 mas per degree of the angular separation (e.g., Reid et al. 2017). Given that the maximum angular separation between our targets and their phase calibrators is $3^\circ.2$, our systematic errors are expected to be ≤ 0.32 mas. These systematic errors were calculated specifically for each detected target source. Overall, we note that the position errors for weak sources ($S_{\nu, \text{peak}} < 200 \mu\text{Jy beam}^{-1}$) are dominated by the statistical errors, and for the strongest sources, they are dominated by the systematic residual phase errors.

3. Results

Radio emission was detected for ten of our 31 targets. The properties of the final images and the flux densities are listed in Table 3, and the positions of the radio sources are given in Table 4.

In the plots of Figure 1, we show an example of a detected radio source, and the remaining images of other detected radio sources are shown in Figure A.1. In most cases, single sources are detected in the images. A possible exception is source HD 199143, where two emission peaks separated by a few milli-arcseconds are detected in the first epoch. Given the low signal-to-noise ratio of the second peak, however, it is not possible to clearly establish that the second peak is a real source. Sources HD 82558 and HD 82159 are single sources in both epochs, but their positions change appreciably from one epoch to the next due to their high proper motion. As mentioned earlier, the combined image aligns both epochs to the position in the first image. The radio sources are rapidly variable, and in several cases, their flux density changes by a factor larger than two in a few days. This high variability was also noticed in the VLA observation (Launhardt et al. 2022) and is typical of stellar sources with magnetic activity (e.g., Güdel 2002).

Table 3. Image properties and measured fluxes of detected radio sources.

Star ID	Epoch	Noise ($\mu\text{Jy beam}^{-1}$)	Synthesized beam		
			$\theta_{\text{maj}} \times \theta_{\text{min}}; \text{P.A.}$ (mas \times mas; $^\circ$)	$S_{\nu, \text{Int.}}$ (μJy)	$S_{\nu, \text{Peak.}}$ ($\mu\text{Jy beam}^{-1}$)
V 875 Per	B1	26	$3.1 \times 1.3; -5.9$	1042 ± 66	585 ± 26
	B2	42	$4.5 \times 1.7; -9.0$	1225 ± 86	885 ± 42
	B1+B2	23	$3.3 \times 1.4; -6.5$	1156 ± 56	667 ± 23
HD 22213	C1	24	$3.6 \times 1.3; +1.5$	338 ± 88	142 ± 24
	C2	26	$3.5 \times 1.1; +9.7$	710 ± 54	552 ± 26
	C1+C2	17	$3.9 \times 1.4; +9.9$	450 ± 40	297 ± 17
HD 285281	D1	17	$4.0 \times 1.7; -6.1$	270 ± 62	96 ± 17
	D2	24	$3.9 \times 1.6; -3.6$	152 ± 47	141 ± 26
	D1+D2	13	$3.9 \times 1.6; -4.9$	170 ± 33	103 ± 13
AI Lep	F1	26	$4.7 \times 1.8; +6.7$	541 ± 59	387 ± 27
	F2	15	$5.0 \times 1.8; +0.1$	105 ± 33	69 ± 15
	F1+F2	12	$4.8 \times 1.8; +1.9$	220 ± 36	144 ± 16
HD 62237	G1	21	$4.3 \times 1.6; -1.8$	415 ± 65	190 ± 21
	G2	19	$4.3 \times 1.6; -0.2$	172 ± 35	164 ± 19
	G1+G2	15	$4.3 \times 1.6; -1.0$	280 ± 38	162 ± 15
SAO 135659	G1	20	$4.2 \times 1.6; -2.7$	648 ± 41	540 ± 21
	G2	22	$4.2 \times 1.7; -0.4$	524 ± 41	444 ± 22
	G1+G2	16	$4.2 \times 1.7; -1.6$	586 ± 31	489 ± 16
HD 82159	H1	66	$3.9 \times 1.6; +3.2$	980 ± 138	734 ± 66
	H2	47	$4.0 \times 1.7; +1.5$	470 ± 76	503 ± 47
	H1+H2	38	$3.9 \times 1.6; +2.2$	669 ± 74	577 ± 39
HD 82558	H1	38	$4.0 \times 1.6; +0.8$	462 ± 77	362 ± 38
	H2	25	$4.2 \times 1.6; -1.2$	219 ± 40	230 ± 25
	H1+H2	22	$4.1 \times 1.6; -0.3$	365 ± 65	260 ± 27
HD 199143	J1	30	$5.1 \times 1.9; -5.4$	280 ± 81	155 ± 31
	J2	20	$5.7 \times 1.6; -9.7$	162 ± 57	81 ± 20
	J1+J2	17	$5.4 \times 1.7; -8.2$	221 ± 64	113 ± 17
GJ 4199	K1	19	$4.0 \times 1.8; -15.9$	350 ± 47	210 ± 19
	K2	24	$4.0 \times 1.8; -12.0$	273 ± 51	192 ± 24
	K1+K2	14	$4.0 \times 1.8; -13.8$	306 ± 33	204 ± 15

Notes. Columns are (from left to right) the target star name, the epoch (for this table the epoch ID is constructed using the group name and the epoch number from Table 2), the image noise level, the synthesized beam size in units of milli-arcseconds, and the integrated and peak flux densities.

Table 4. Astrometry of detected radio sources.

Star ID	Epoch	R.A.	σ_α	Dec	σ_δ	$\Delta\alpha_{\text{radio}}^*$	$\Delta\delta_{\text{radio}}$	$\Delta\theta_{\text{radio}}$	$\Delta\alpha^*$	$\Delta\delta$	$\Delta\theta$	σ_{sys}	$\Delta\lambda$
(1)	(2)	(3)	(μs)	(5)	(μas)	($''$)	($''$)	($''$)	(mas)	(mas)	(mas)	(mas)	(au)
V 875 Per	B1	02 ^h 52 ^m 17 ^s .687958	3.3	+36°16'47".407545	60	0.06 ± 0.10	0.02 ± 0.07	0.06 ± 0.10	0.19 ± 0.16	-0.61 ± 0.12	0.6 ± 0.1	0.14	0.10 ± 0.06
	B2	02 ^h 52 ^m 17 ^s .687982	3.8	+36°16'47".407500	85								
	B1+B2	02 ^h 52 ^m 17 ^s .687968	2.7	+36°16'47".407501	49								
HD 22213	C1	03 ^h 34 ^m 16 ^s .458216	22	-12°04'08".026964	374	-0.09 ± 0.10	-0.07 ± 0.14	0.11 ± 0.12	-1.0 ± 0.3	+0.2 ± 0.4	1.1 ± 0.3	0.11	0.05 ± 0.02
	C2	03 ^h 34 ^m 16 ^s .458292	1.9	-12°04'08".026581	79								
	C1+C2	03 ^h 34 ^m 16 ^s .458287	2.5	-12°04'08".026752	98								
HD 285281	D1	04 ^h 00 ^m 31 ^s .076436	14	+19°35'20".650376	580	-0.19 ± 0.18	0.04 ± 0.19	0.19 ± 0.18	+0.3 ± 0.2	+0.8 ± 0.6	0.9 ± 0.5	0.16	0.12 ± 0.06
	D2	04 ^h 00 ^m 31 ^s .076421	8.6	+19°35'20".648346	332								
	D1+D2	04 ^h 00 ^m 31 ^s .076421	7.2	+19°35'20".649016	317								
AI Lep	F1	05 ^h 40 ^m 20 ^s .759902	4.8	-19°40'11".183095	152	0.55 ± 0.37	0.32 ± 0.42	0.64 ± 0.39	+0.2 ± 0.1	+0.4 ± 0.2	0.5 ± 0.1	0.10	0.04 ± 0.01
	F2	05 ^h 40 ^m 20 ^s .759861	18	-19°40'11".182392	465								
	F1+F2	05 ^h 40 ^m 20 ^s .759892	8.6	-19°40'11".182835	238								
HD 62237	G1	07 ^h 42 ^m 26 ^s .562160	8.4	-16°17'00".668793	321	-0.11 ± 0.12	0.11 ± 0.23	0.16 ± 0.19	+12.3 ± 0.5	-23.6 ± 0.6	26.6 ± 0.6	0.10	3.32 ± 0.08
	G2	07 ^h 42 ^m 26 ^s .562170	5.8	-16°17'00".668809	230								
	G1+G2	07 ^h 42 ^m 26 ^s .562169	6.0	-16°17'00".668891	214								
SAO 135659	G1	08 ^h 13 ^m 50 ^s .953026	1.9	-07°38'25".622119	76	-0.04 ± 0.03	0.04 ± 0.03	0.06 ± 0.03	-10.5 ± 1.2	-72.6 ± 1.0	73.3 ± 1.0	0.14	3.67 ± 0.06
	G2	08 ^h 13 ^m 50 ^s .953037	2.3	-07°38'25".622112	98								
	G1+G2	08 ^h 13 ^m 50 ^s .953031	1.7	-07°38'25".622091	65								
HD 82159	H1	09 ^h 30 ^m 35 ^s .542606	5.5	+10°36'05".979934	151	-0.04 ± 0.03	0.02 ± 0.03	0.04 ± 0.03	-1.24 ± 0.2	+0.2 ± 0.2	1.3 ± 0.2	0.18	0.05 ± 0.01
	H2	09 ^h 30 ^m 35 ^s .542401	4.6	+10°36'05".979351	145								
	H1+H2								
HD 82558	H1	09 ^h 32 ^m 25 ^s .204609	5.9	-11°11'03".942747	185	-0.07 ± 0.29	0.03 ± 0.45	0.07 ± 0.31	-0.6 ± 0.2	+0.2 ± 0.2	0.7 ± 0.2	0.06	0.010 ± 0.003
	H2	09 ^h 32 ^m 25 ^s .204348	4.9	-11°11'03".940469	183								
	H1+H2								
HD 199143	J1	20 ^h 55 ^m 47 ^s .759095	20	-17°06'52".304352	441	0.47 ± 0.15	0.48 ± 0.15	0.67 ± 0.15	-2.6 ± 0.3	+3.6 ± 0.5	4.4 ± 0.4	0.27	0.20 ± 0.02
	J2	20 ^h 55 ^m 47 ^s .759173	24	-17°06'52".305210	608								
	J1+J2	20 ^h 55 ^m 47 ^s .759121	15	-17°06'52".304406	333								
GJ 4199	K1	21 ^h 31 ^m 01 ^s .925936	9.2	+23°20'04".291167	144	0.05 ± 0.05	-0.06 ± 0.05	0.08 ± 0.05	0.6 ± 0.1	+1.3 ± 0.2	1.4 ± 0.2	0.19	0.03 ± 0.01
	K2	21 ^h 31 ^m 01 ^s .925974	11	+23°20'04".291129	190								
	K1+K2	21 ^h 31 ^m 01 ^s .925953	6.7	+23°20'04".291177	112								

Notes. Columns are (from left to right) the target name, epoch ID as in Table 3, measured positions in the VLBA images and their statistical errors derived from JMFIT, and the estimated offset between the radio source detected with the VLA and the radio source detected with the VLBA ($\Delta\alpha_{\text{radio}}^*$, $\Delta\delta_{\text{radio}}$, and $\Delta\theta_{\text{radio}}$). The offsets $\Delta\alpha^*$, $\Delta\delta$, and $\Delta\theta$ are the angular separations between the radio source (VLBA) and the *Gaia* DR3 predicted position at the observed epoch in right ascension, declination, and total, respectively. The column σ_{sys} is the position systematic error expected from the phase difference of the target and its phase calibrator, given their angular separation. Finally, column $\Delta\lambda$, which is derived from $\Delta\theta$, is the linear separation in astronomical units at the corresponding distance (see Table 1).

4. Discussion

4.1. Comparison with VLA results

The radio sources associated with our target stars are listed in Table 1 and were first reported by Launhardt et al. (2022). These authors measured the variability of the radio sources and pointed out that they are nonthermal emitter candidates, motivating the follow-up VLBA observations presented here. We confirm the nonthermal nature of the radio sources detected with the VLBA, as they require brightness temperatures $> 10^6$ K to be detected with interferometric baselines of $\sim 8\,000$ km (see chapter 9 of Thompson et al. 2017). These brightness temperatures are a strong indication of the nonthermal radio emission associated with young stars (Feigelson & Montmerle 1999).

The angular resolution of VLA images presented by Launhardt et al. (2022) is $\sim 2''$, which is insufficient to resolve potential tight binaries. As an example, in the case of EC 95 in Serpens, VLA observations showed the presence of a single radio source (Eiroa et al. 2005). Follow-up VLBA observations showed that the radio source is a hierarchical triple sys-

tem, with three nonthermal variable radio emitters unresolved at the VLA angular resolution. The first VLBA observations of EC 95 showed a close binary with an angular separation of about 15 mas (Dzib et al. 2010), and later a third radio source was detected at an angular distance of about 140 mas from the close binary (Ortiz-León et al. 2017a). Because of their variability, not all components were detected in all observed epochs. Thus, whether the radio sources detected in this work are identical to the radio sources reported by Launhardt et al. (2022) needs to be analyzed. Indeed, the analysis by Launhardt et al. (2022) showed that, in some cases, the radio emission can have contributions from both components in known binary systems or be related to an unknown companion.

For our analysis, we compared the positions derived from the VLBA and the VLA. First, we assumed that the radio sources share the trigonometric parallax and proper motions of the associated stars reported by *Gaia* (see Table 1) to extrapolate the positions reported from the VLA observations to the epoch of the corresponding first VLBA observation. Then, we computed the offset between the position determined by the VLBA ob-

servations and the extrapolated position from VLA observations ($\Delta\alpha_{\text{radio}}$, $\Delta\delta_{\text{radio}}$ and $\Delta\theta_{\text{radio}}$). The position offsets of these radio observations are listed in columns (7) to (9) of Table 4 and are shown graphically in Figures 2 and B.1. Given the differences in angular resolution, the dominant error in the position offsets is the VLA position error, which is two orders of magnitude larger than those from the VLBA.

The offsets between the VLA and VLBA positions are less than three times the errors for nine out of the ten detected sources. In these cases, the VLA and VLBA radio sources presumably correspond to the same emitting source. In the case of HD 199143, the separation is larger than three times the errors. This indicates that the radio source detected with the VLBA corresponds to a different object than the one reported from VLA observations. Launhardt et al. (2022) argued that the radio source detected in the VLA observations is positionally consistent with the expected position of the fainter companion, HD 199143 B (not in the *Gaia* DR3 catalog), located 0''.84 northwest of the main stellar component (Hagelberg et al. 2020, see also Fig. 2). In the next section, we show that the radio source detected in the VLBA images corresponds to the primary stellar component in this system or to a very nearby companion.

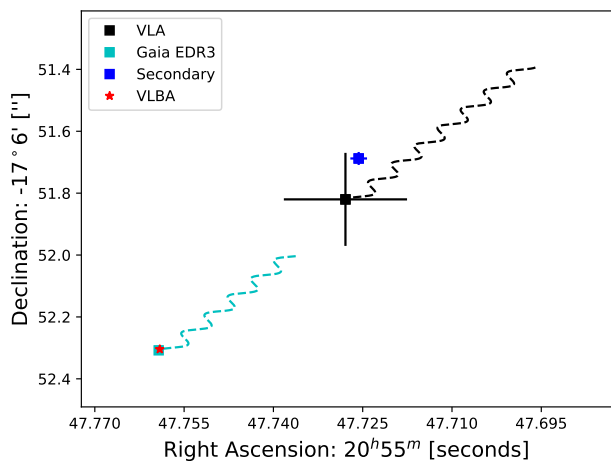


Fig. 2. Positions of the radio and optical sources related to HD 199143. The red star indicates the position of the radio source in the first detected epoch by the VLBA observations. The Cyan dashed line indicates the optical trajectory of the primary component of the HD 199143 stellar system from 2016.0 to the epoch of detection of the radio source with the VLBA. The optical position of the star at the VLBA observed epoch is indicated with the cyan square. The blue square indicates the position of the secondary, HD 199143 B, whose absolute coordinates are unknown. Coordinates relative to the primary from the WDS catalog were used to estimate the absolute position. *Gaia* DR3 and VLBA position errors are smaller than the symbol sizes. The black line is the trajectory followed by the radio source detected with the VLA (Launhardt et al. 2022), assuming the derived astrometry at optical wavelengths from the VLA observed epoch to the VLBA observed epoch. The black square indicates the extrapolated position of the VLA radio source at the epoch of the VLBA detection. The black cross size indicates the VLA positional error.

4.2. Comparison with optical astrometry

To examine the relationship between the radio sources detected with the VLBA and the targeted stars, we have used the astrometric results from optical wavelengths (i.e., *Gaia*) to determine the stellar positions at the epoch of the VLBA observations. Then, we determined the angular offsets between the radio source and

the optical counterpart ($\Delta = \text{Pos}_{\text{radio}} - \text{Pos}_{\text{opt}}$). The initial parameter uncertainties (optical: position, proper motion, and parallax; radio: position) were propagated to estimate the angular separation error by using a Monte Carlo approach. In columns 10, 11, and 12 of Table 4, we list the angular separation in right ascension, $\Delta\alpha^* = \Delta\alpha \cdot \cos(\text{Dec.})$ and in declination, ($\Delta\delta$), and the total angular separation ($\Delta\theta$) between the VLBA and optical sources. Expected systematic errors in the source position caused by residual phase calibration errors are listed in column 11 and were added quadratically to the errors provided by JMFIT.

Seven of the ten radio sources are consistent with the expected position from *Gaia* results within five times the errors. We argue that, in these cases, the radio emission is tracing the stellar corona of the stars seen at optical wavelengths. Stellar coronae of young stars could be of sizes up to $10 R_*$ (see the review by Güdel 2002). For a conservative value for the stellar radii, we assumed $1 R_* = 1.15 R_\odot$, as the observed stars are of spectral types F8 or later and about to enter the main sequence. At the distances of our targets, this implies angular sizes of less than 2.9 mas. On the other hand, the measured positions of the other three radio sources (HD 62237, SAO 135659, and HD 199143) are not consistent with the results from *Gaia*, and the offset cannot be attributed to the stellar coronae structure, as they would require structures greater than $40 R_*$.

To look for clues on the origin of the radio-optical position discrepancies in these three sources, we first turned to the *Gaia* results. The *Gaia* catalog includes a measure of the quality of the astrometric fits called the renormalized unit weight error (RUWE; listed Table 5 for our targets). The RUWE index is expected to be close to 1.0 for stars whose motion is well described by a uniform linear motion, while a large RUWE value (> 1.4) indicates a significant deviation from a linear uniform motion and is suggestive of the presence of an unseen companion. Interestingly, two of the three sources where we found discrepancies between the VLBA and optical positions (HD 62237 and SAO 135659) have very large RUWE values (7.3 and 13.8, respectively). A second relevant piece of information is provided by the proper motion anomaly (PMA) introduced by Kervella et al. (2019) and Kervella et al. (2022) and listed in the fifth column of Table 5. The PMA quantifies discrepancies between the proper motions measured by the Hipparcos and *Gaia* astrometric missions. A large PMA indicates significantly different proper motions in the Hipparcos and *Gaia* catalogs and suggests the presence of a low-mass companion with an orbital period larger than the *Gaia* observation window (668 days for *Gaia* DR3). The third source where we found a discrepancy between the VLBA and optical positions (HD 199143) has a very large PMA (56.7).

In summary, the three sources where the VLBA and optical positions do not coincide have astrometric evidence of multiplicity. In contrast, the sources where the VLBA and optical positions do coincide have RUWE values close to unity and either small PMA values or no PMA at all.

Given the evidence presented above that the sources with discrepant VLBA and optical positions are multiple, our next step was to look for known companions. We searched the Washington Visual Double Star Catalog (WDS; Mason et al. 2001, 2022) for companions to our target stars.² We list the stellar companions and their angular separation in Table 5. In cases where there is more than one known companion, we include only the companion with the smallest angular separation to the targeted star. For HD 62237 and HD 199143, the angular separation of the visual

² For completeness, we searched the WDS catalog for companions to all of our targets, not just for HD 62237, SAO 135659, and HD 199143.

Table 5. Previous companion information.

Star ID	Companion Name	Angular separation	$\Delta\theta$ (mas)	PMa ^a (SNR)	RUWE	SORS ^b	SORS This work
V 875 Per	WDS 02523+3617 B ^c	5''4	0.6 ± 0.2	...	1.2	Main	Main
HD 22213	WDS 03343–1204 B	1''7	1.1 ± 0.3	...	1.1	Main	Main
HD 285281	WDS 04005+1935 B	0''8	0.9 ± 0.5	...	1.5	Main	Main
AlLep	WDS 05403–1940 B	8''4	0.5 ± 0.2	...	1.0	Main	Main
HD 62237	26.6 ± 0.6	...	7.3	Main	New companion
SAO 135659	WDS 08138–0738 B	0''1	73.3 ± 1.0	...	13.8	Main/Companion	Companion
HD 82159	WDS 09306+1036 B	13''8	1.3 ± 0.3	1.74	1.6	Main	Main
HD 82558	0.7 ± 0.2	0.79	1.1	Main	Main
HD 199143	HD 199143 B	0''84	4.4 ± 0.5	56.68	1.0	Companion	New Companion
GJ 4199	WDS 21310+2320 B	9''2	1.4 ± 0.3	0.99	1.0	Main	Main

Notes. Angular separations of previously known companions are from the Washington Visual Double Star Catalog (Mason et al. 2001, 2022), except for HD 199143, which is from (Hagelberg et al. 2020). The quoted error value in $\Delta\theta$ was estimated by adding in quadrature the statistic and systematic errors listed in Table 4.

Sources discussed further in the text are highlighted.

^(a) As reported by Kervella et al. (2019) or Kervella et al. (2022). ^(b) Suggested origin of the radio source (SORS) as reported by Launhardt et al. (2022). ^(c) No physical companion (Mason et al. 2022).

binaries is much larger than the VLBA-optical astrometric discrepancy $\Delta\theta$. In the case of SAO 135659, however, the values are comparable. We come back to this point momentarily. We also investigated if our targets had been reported as spectroscopic binaries. Four of our target sources (HD 22213, SAO 135659, GJ 4199, and HD 199143) were included in the spectroscopic analysis by Zúñiga-Fernández et al. (2021). Only HD 22213 was confirmed as a spectroscopic binary. In particular, none of the stars with discrepant optical and VLBA positions are a known spectroscopic binary.

Armed with the information gathered for each system, we are now in a position to discuss the three targets where the VLBA and optical positions do not coincide. Particularly, we discuss if the origin of the position discrepancy can be explained by known companions.

Firstly, SAO 135659 is known to be a binary star with stellar components of similar masses (0.77 and 0.64 M_{\odot} for the primary and secondary, respectively). The angular separation of the system is $\sim 0''1$ almost in the north-south direction at the epoch of the observations reported by Elliott et al. (2015). At a distance of 50 pc and given the total mass, we can estimate the period of the system to be roughly 9 years. Coincidentally, this is similar to the separation between the observations realized by Elliott et al. (2015) in May 2012 and our VLBA observations in April 2021. Consequently, we expect the relative offset between the two stars to also be on order of $\sim 0''1$ in the north-south direction at the time of our VLBA observations. In our observations, the position of the VLBA source was found to be located about $\sim 0''07$ north of the expected *Gaia* position (Fig. B.1). The similarity between the relative position of the optical and VLBA sources and the expected relative positions of the two stars in SAO 135659 strongly suggests that the VLBA source is associated with the secondary (WDS 08138-0738). The small difference in separation ($\sim 0''1$ vs. $\sim 0''07$) could easily be caused by the somewhat different orbit phase seen during our observations compared to those of Elliott et al. (2015) and by the fact that *Gaia* presumably traces the position of the photocenter of the system rather than the exact position of the primary.

The source HD 199143 exhibits a large PMa. The detailed analysis from Launhardt et al. (2022) shows that this can be explained

by the known companion HD 199143 B located at $\sim 0''84$ (see Fig. 12 from Launhardt et al. 2022). The VLA source reported by Launhardt et al. (2022) coincides with that companion (see also Fig. 2). The VLBA source we detect here, however, is located very near the primary of the system (Fig. 2). The small but significant offset between the VLBA position and the expected position of the primary (4.4 ± 0.5 mas) could be due to the presence of another hitherto undetected companion located very close to the primary. Given the small offset, however, further observations will be needed. To finish on this source, we note that we searched for a second VLBA radio source in the expected position of the companion but found none. The flux of the companion star was below $110 \mu\text{Jy beam}^{-1}$ (6.5 times the noise level in our image) during the VLBA observations. The radio source detection by Launhardt et al. (2022) and the one reported here is interesting but unsurprising, and it points to the highly variable nature of the radiation mechanisms in magnetically active stars (e.g., Güdel 2002).

Regarding HD 62237, it has no known companion, but the large *Gaia* RUWE value strongly suggests that such a companion exists. We argue that the VLBA source, offset by about 27 mas from the expected position of the primary, traces that companion. We note that, given the modest resolution of the VLA observations reported by Launhardt et al. (2022), the VLA source could coincide with either the primary or the secondary putatively traced by the VLBA (Fig. 2). This companion should be less luminous than the primary star, as a clear offset between the *Gaia* and VLBA positions indicates that the system photocenter is coincident or close to the primary star. However, the mass of the companion must be significant to cause the linear fitting by *Gaia* DR3 to not properly describe the motion of the system (RUWE value is 7.3). The spectral type of HD 62237 is G5V, indicating a star with a mass of 0.93 M_{\odot} (Zombeck 1990). Assuming that the companion has a mass between 0 and 0.5 M_{\odot} , the mass of the system ranges from 0.93 to 1.43 M_{\odot} . We also assume that the optical-radio offset of 26.6 ± 0.6 mas (3.32 ± 0.08 au at a distance of 124.76 pc) is the semi-major axis of the orbit, and we roughly estimate an orbital period of the system in the range from 5.1 to 6.3 years.

5. Conclusions

We have presented a series of VLBA observations of a sample of 31 nearby young stars previously reported as radio sources, obtaining ten detections (for a detection rate on the order of 30%). The radio sources are compact at our angular resolution of a few milli-arcseconds and are highly variable; both properties confirm they are nonthermal radio emitters. All detected radio sources are associated with stars with good astrometry from *Gaia* DR3. Using these results, we extrapolated the position of the optical stars to the epoch of the radio observations to compare the radio and optical positions. For seven of the ten detected radio sources, the optical and radio positions are consistent. Three radio sources, however, have position discrepancies above eight times the errors. All three of these sources show independent evidence of multiplicity, and we attribute the position discrepancies to the presence of companions.

Follow-up observations of the detected radio sources will be of high interest for comparison with *Gaia* astrometry. Such observations could provide some clues on the *Gaia* parallax zero point and on the relative orientation of the *Gaia* and ICRF reference frames by increasing the current numbers of stars with *Gaia*- and VLBI-derived astrometry.

Acknowledgements. We thank the anonymous referee for his/her careful review and insightful comments. We thank Eduardo Ros for reading the paper and providing suggestions that improve the readability of the paper. S.A.D. acknowledges the M2FINDERS project from the European Research Council (ERC) under the European Union's Horizon 2020 research and innovation programme (grant No 101018682). L.L. acknowledges the support of UNAM-DGAPA PA-PIIT grants IN108324 and IN112820 and CONACYT-CF grant 263356. J.O.-T. acknowledges a stipend from CONAHCYT, México. The National Radio Astronomy Observatory is a facility of the National Science Foundation operated under cooperative agreement by Associated Universities, Inc. This work has made use of data from the European Space Agency (ESA) mission *Gaia* (<https://www.cosmos.esa.int/gaia>), processed by the *Gaia* Data Processing and Analysis Consortium (DPAC, <https://www.cosmos.esa.int/web/gaia/dpac/consortium>). Funding for the DPAC has been provided by national institutions, in particular the institutions participating in the *Gaia* Multilateral Agreement.

References

Beasley, A. J. & Conway, J. E. 1995, in *Astronomical Society of the Pacific Conference Series*, Vol. 82, *Very Long Baseline Interferometry and the VLBA*, ed. J. A. Zensus, P. J. Diamond, & P. J. Napier, 327

Bell, C. P. M., Mamajek, E. E., & Naylor, T. 2015, *MNRAS*, 454, 593

Briggs, D. S. 1995, PhD thesis, New Mexico Institute of Mining and Technology, United States

Carpenter, J. M., Bouwman, J., Mamajek, E. E., et al. 2009, *ApJS*, 181, 197

da Silva, L., Torres, C. A. O., de La Reza, R., et al. 2009, *A&A*, 508, 833

Desidera, S., Covino, E., Messina, S., et al. 2015, *A&A*, 573, A126

Dzib, S., Loinard, L., Mioduszewski, A. J., et al. 2010, *ApJ*, 718, 610

Dzib, S. A., Forbrich, J., Reid, M. J., & Menten, K. M. 2021, *ApJ*, 906, 24

Eiroa, C., Torrelles, J. M., Curiel, S., & Djupvik, A. A. 2005, *AJ*, 130, 643

Elliott, P., Huélamo, N., Bouy, H., et al. 2015, *A&A*, 580, A88

Feigelson, E. D. & Montmerle, T. 1999, *ARA&A*, 37, 363

Forbrich, J., Dzib, S. A., Reid, M. J., & Menten, K. M. 2021, *ApJ*, 906, 23

Gaia Collaboration, Brown, A. G. A., Vallenari, A., et al. 2021, *A&A*, 649, A1

Gaia Collaboration, Prusti, T., de Bruijne, J. H. J., et al. 2016, *A&A*, 595, A1

Gaia Collaboration, Vallenari, A., Brown, A. G. A., et al. 2023, *A&A*, 674, A1

Galicher, R., Marois, C., Macintosh, B., et al. 2016, *A&A*, 594, A63

Galli, P. A. B., Loinard, L., Bouy, H., et al. 2019, *A&A*, 630, A137

Greisen, E. W. 2003, in *Astrophysics and Space Science Library*, Vol. 285, *Information Handling in Astronomy - Historical Vistas*, ed. A. Heck, 109

Güdel, M. 2002, *ARA&A*, 40, 217

Hagelberg, J., Engler, N., Fontanive, C., et al. 2020, *A&A*, 643, A98

Høg, E., Fabricius, C., Makarov, V. V., et al. 2000, *A&A*, 355, L27

Kenyon, S. J. & Hartmann, L. 1995, *ApJS*, 101, 117

Kervella, P., Arenou, F., Mignard, F., & Thévenin, F. 2019, *A&A*, 623, A72

Kervella, P., Arenou, F., & Thévenin, F. 2022, *A&A*, 657, A7

Launhardt, R., Loinard, L., Dzib, S. A., et al. 2022, *ApJ*, 931, 43

Lestrade, J. F., Preston, R. A., Jones, D. L., et al. 1999, *A&A*, 344, 1014

Lestrade, J. F., Rogers, A. E. E., Whitney, A. R., et al. 1990, *AJ*, 99, 1663

Lindgren, L. 2020, *A&A*, 633, A1

Lindgren, L., Hernández, J., Bombrun, A., et al. 2018, *A&A*, 616, A2

Loinard, L., Mioduszewski, A. J., Rodríguez, L. F., et al. 2005, *ApJ*, 619, L179

Loinard, L., Torres, R. M., Mioduszewski, A. J., et al. 2007, *ApJ*, 671, 546

Mason, B. D., Wycoff, G. L., Hartkopf, W. I., Douglass, G. G., & Worley, C. E. 2001, *AJ*, 122, 3466

Mason, B. D., Wycoff, G. L., Hartkopf, W. I., Douglass, G. G., & Worley, C. E. 2022, *VizieR Online Data Catalog*, B/wds

Montes, D., López-Santiago, J., Gálvez, M. C., et al. 2001, *MNRAS*, 328, 45

Ortiz-León, G. N., Dzib, S. A., Kounkel, M. A., et al. 2017a, *ApJ*, 834, 143

Ortiz-León, G. N., Loinard, L., Dzib, S. A., et al. 2018, *ApJ*, 869, L33

Ortiz-León, G. N., Loinard, L., Kounkel, M. A., et al. 2017b, *ApJ*, 834, 141

Reid, M. J. & Brunthaler, A. 2004, *ApJ*, 616, 872

Reid, M. J., Brunthaler, A., Menten, K. M., et al. 2017, *AJ*, 154, 63

Reid, M. J. & Honma, M. 2014, *ARA&A*, 52, 339

Riess, A. G., Casertano, S., Yuan, W., et al. 2018, *ApJ*, 861, 126

Stanford-Moore, S. A., Nielsen, E. L., De Rosa, R. J., Macintosh, B., & Czekała, I. 2020, *ApJ*, 898, 27

Thompson, A. R., Moran, J. M., & Swenson, George W., J. 2017, *Interferometry and Synthesis in Radio Astronomy*, 3rd Edition

van Leeuwen, F. 2007, *A&A*, 474, 653

Weise, P., Launhardt, R., Setiawan, J., & Henning, T. 2010, *A&A*, 517, A88

Xu, S., Zhang, B., Reid, M. J., Zheng, X., & Wang, G. 2019, *ApJ*, 875, 114

Zinn, J. C., Pinsonneault, M. H., Huber, D., & Stello, D. 2019, *ApJ*, 878, 136

Zombeck, M. V. 1990, *Handbook of space astronomy and astrophysics*

Zúñiga-Fernández, S., Bayo, A., Elliott, P., et al. 2021, *A&A*, 645, A30

Appendix A: Images of detected radio sources

We detected ten of our 31 targets. The obtained images from our VLBA observations are presented in this appendix. The plots in Figure A.1 are the intensity maps of nine detected radio sources; the remaining source is presented in the main text. The figures include the expected positions of the stars at the epochs of the VLBA observations as calculated from *Gaia* DR3 (Gaia Collaboration et al. 2021, 2023).

To produce the images combining the data from both epochs, we corrected the position of the second epoch, assuming that the optical astrometric parameters could be applied to the radio observations. In AIPS, this was done with the task *CLCOR* using the operation code *ANTC*. The position correction for each target was performed by specifying the offsets in right ascension and declination in arcsecond units ($clcorprm(5,6) = \alpha_{\text{offset}}, \delta_{\text{offset}}$). The values of these offsets are listed in Table A.1.

We assumed the upper limits for the nondetected sources to be 6.5 times the noise levels of images where the two observed epochs of each source were combined. These noise level values are also listed in Table A.1.

Table A.1. Offsets applied to combine data of the two observed epochs and the noise level of the obtained image.

Star ID	Offsets (mas)		Noise $\mu\text{Jy bm}^{-1}$
	α	δ	
BD17232	-0.45	+0.13	25
HIP 12545	-0.30	+0.22	13
HIP 12635	-0.41	+0.89	14
V 875 Per	-0.32	+0.27	23
TYC 3301	-0.37	+0.79	15
HD 22213	-0.55	-0.23	17
HD 23524	-0.44	+0.76	19
HD 24681	-0.21	+0.43	12
HD 285281	+0.02	+0.07	13
HD 284135	+0.05	+0.11	14
HD 31281	-0.00	+0.03	21
BD 08995	-0.08	-0.05	16
HD 286264	-0.06	+0.12	16
HD 293857	-0.05	+0.06	15
TYC 7136611	+0.01	+0.25	10
TYC 59251547	-0.04	-0.03	12
AI Lep	-0.04	-0.13	12
HD 62237	+0.05	-0.10	15
SAO 135659	+0.26	-0.15	16
WDS 09035+3750B	+0.42	+4.74	19
HD 82159	+3.42	+0.14	38
HD 82558	+4.01	-3.24	22
GJ 2079	+2.75	+4.44	16
HD 135363	+1.02	-1.03	20
UCAC 4832	+1.02	-1.03	14
HD 199143	-0.37	+0.51	17
HD 358623	-0.38	+0.54	16
SAO 50350	-0.35	-0.93	14
GJ 4199	-0.28	-0.00	14
SAO 51891	-0.43	-0.45	18
SAO 108142	-0.29	+0.05	13

Notes. Offsets are as expected assuming the parallax and proper motions obtained from the optical results. Detected sources are highlighted with gray-shaded rows. The noise value was measured in the image of two combined epochs, that is, after applying the correction of the offsets.

Appendix B: Figures comparing VLBA, VLA, and *Gaia* astrometric results

Figure B.1 shows the measured VLBA position of detected radio sources. In these plots, for comparison, we also show the position of the VLA radio sources detected by Launhardt et al. (2022), where we have extrapolated its position to the epoch of the VLBA observation using the results of optical astrometry. The expected optical position at the epoch of VLBA observations is also shown. Finally, in two cases, SAO 135659 and HD199143, the relative position to the primary of a companion was obtained from the Washington Visual Double Star catalog (Mason et al. 2001, 2022) and are also shown in these plots.

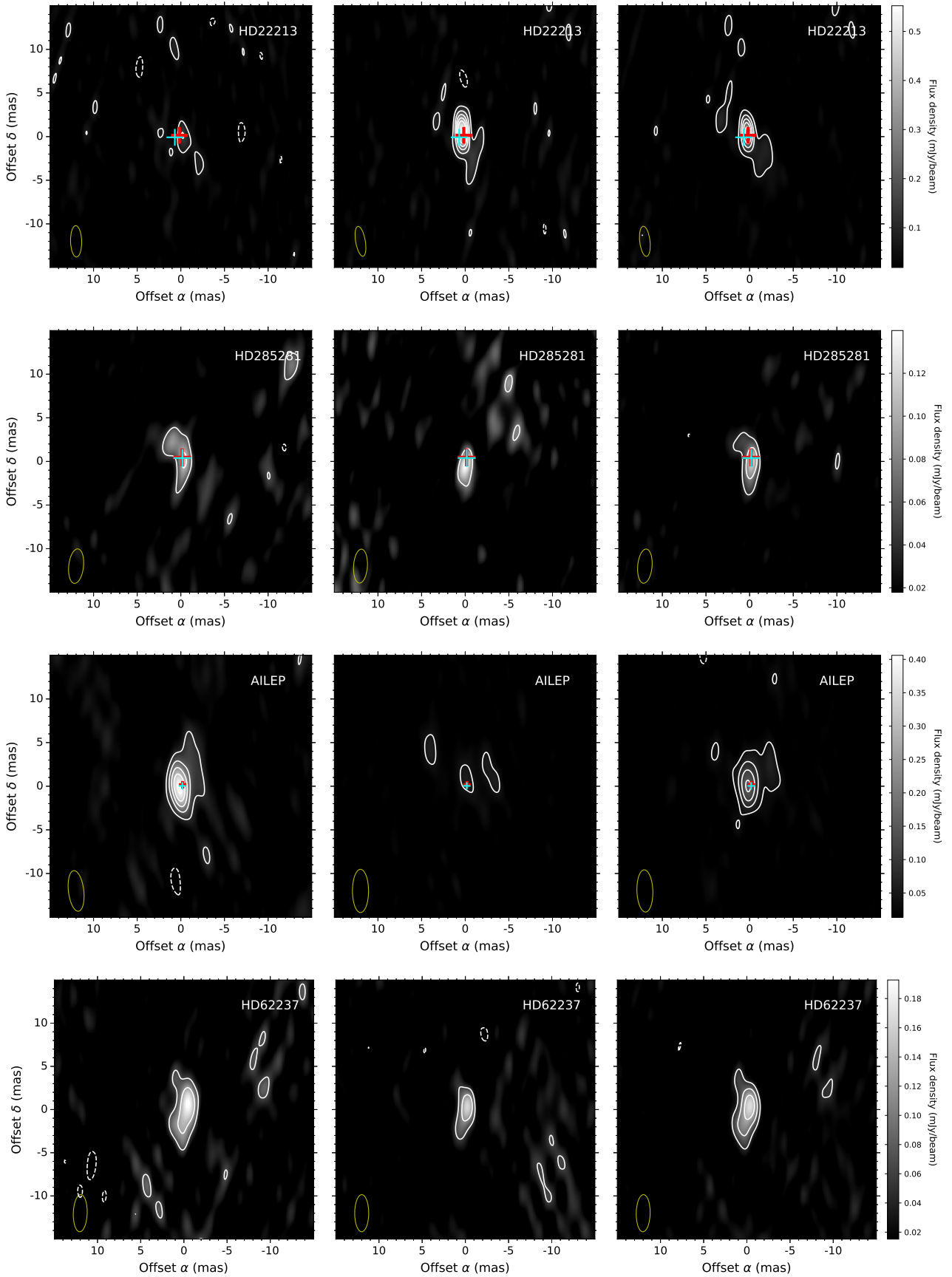


Fig. A.1. VLBA images of detected radio sources. The images are centered in the position of the radio source as detected in the first epoch (see Table 4). The name of the stellar source related to the radio sources is indicated in the top-left corner. The images, from left to right, correspond to the epochs 1, 2, and the combination of both epochs. Contour levels are $-3, 3, 6, 9, 12,$ and 15 times the noise level of the image as listed in Table 3. The yellow open ellipse in the bottom-left corner represents the size of the synthesized beam of the image as listed in Table 3. The predicted optical position in epochs 1 and 2 are shown as red and cyan crosses, respectively. For HD 62237 and SAO 135659, these positions fall outside the region shown, page 10 of 12

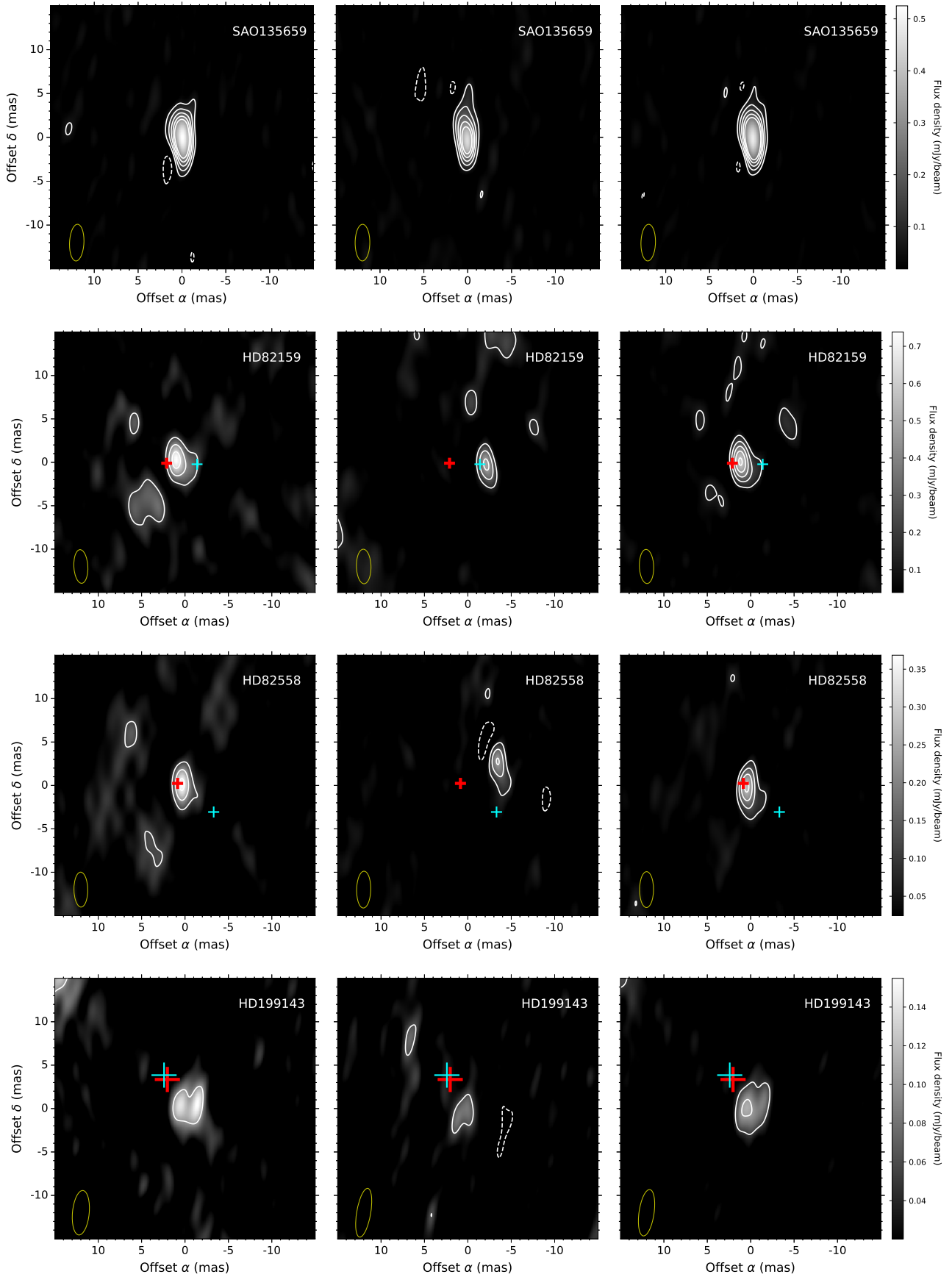


Fig. A.1. Continued.

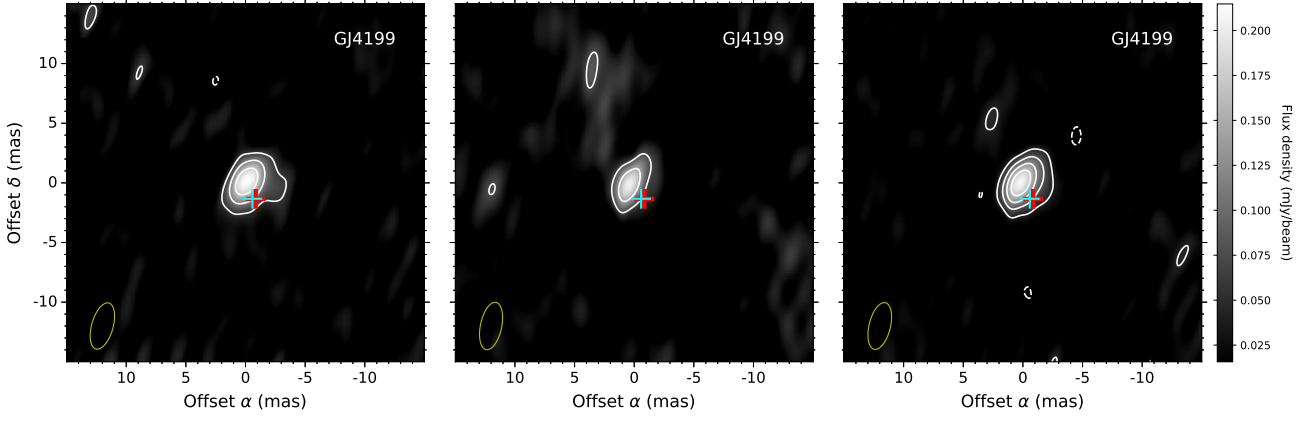
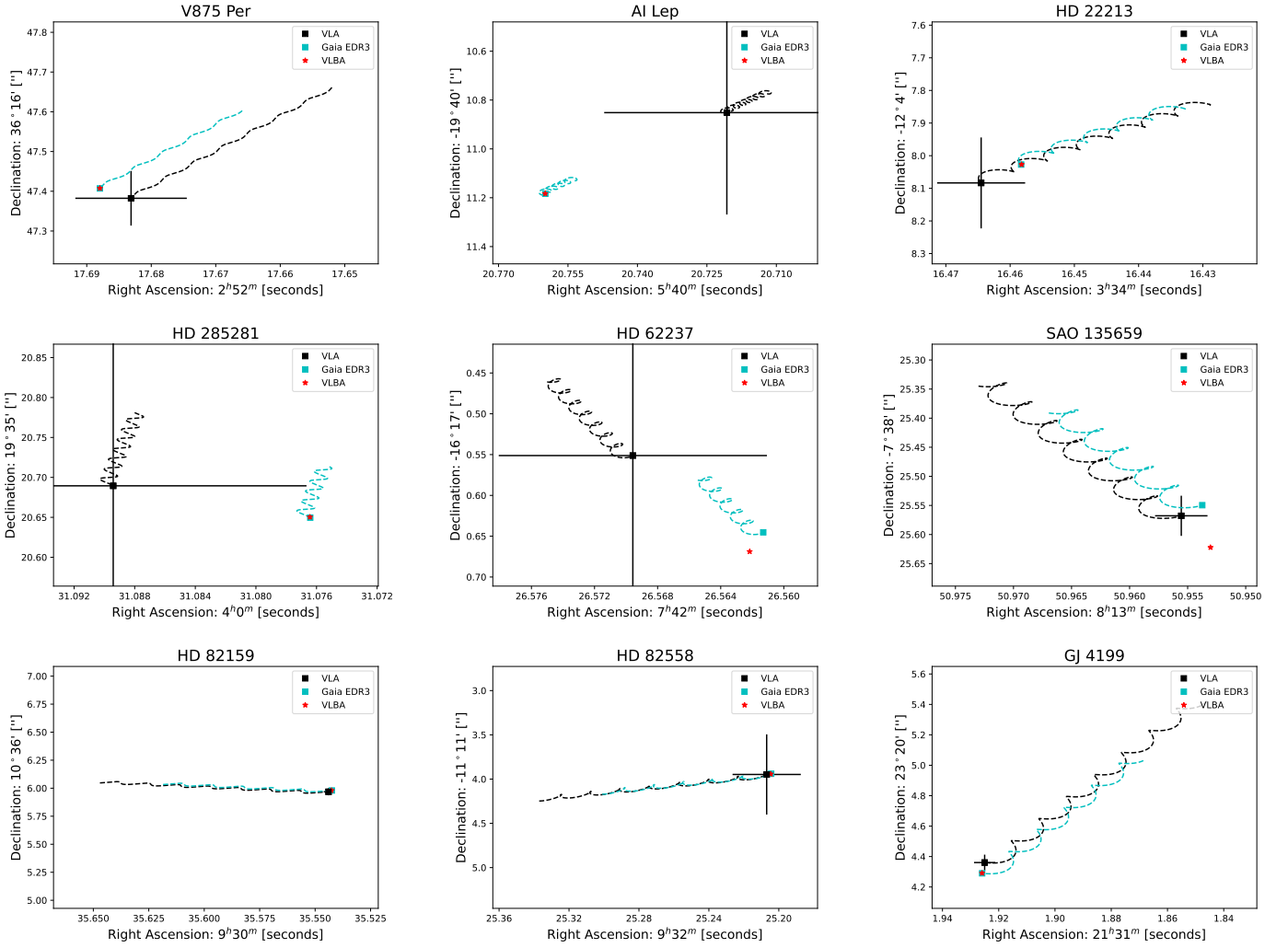

Fig. A.1. Continued.


Fig. B.1. Positions of radio and optical sources related to our target sources. The name of source is indicated at the top of each plot. Red stars indicate the position of the radio source in the first detected epoch by the VLBA observations. The black line is the trajectory followed by the radio source detected with the VLA (Launhardt et al. 2022), assuming the derived astrometry at optical wavelengths (see Table 4) from the VLA observed epoch to the VLBA observed epoch. The black square indicates the extrapolated position of the VLA radio source at the epoch of the VLBA detection. The black cross size indicates the VLA positional error. The cyan line indicates the trajectory of the optical results from 2016.0 to the epoch of detection of the radio source with the VLBA; the position of the optical source at this epoch is indicated with the cyan square. *Gaia* DR3 and VLBA position errors are smaller than the symbol sizes. Companion relative positions are shown as blue squares.